J. Fluid Mech. (2017), *vol.* 824, *pp.* 701–721. © Cambridge University Press 2017
doi:10.1017/jfm.2017.331

The structure of a trailing vortex from a perturbed wing

G. Fishman[1,†], M. Wolfinger[1] and D. Rockwell[1]

[1]Department of Mechanical Engineering, Lehigh University, Bethlehem, PA 18015, USA

(Received 22 August 2016; revised 5 May 2017; accepted 16 May 2017;
first published online 10 July 2017)

The structure of a trailing vortex from a wing undergoing small amplitude, low frequency heaving motion is investigated using space–time representations determined from stereo particle image velocimetry. The evolution of the vortex shows large fluctuations of axial velocity deficit and circulation during the oscillation cycle. Correspondingly, large variations of swirl ratio occur and onset of pronounced azimuthal vorticity arises. At a given cross-section of the vortex, the pattern of azimuthal vorticity moves around its axis in an ordered fashion as both it and the pattern of velocity defect increase in magnitude and scale. When the swirl ratio attains its minimum value during the oscillation cycle, and this value lies below the theoretically established critical threshold for amplification of azimuthal modes, the magnitude and scale of the pattern of azimuthal vorticity is maximized. Subsequent increase of the swirl ratio yields attenuation of the azimuthal vorticity. Onset of pronounced azimuthal vorticity when the swirl ratio decreases involves rapid amplification, then disruption, of axial vorticity fluctuation.

Key words: vortex flows

1. Introduction

The evolution of wing-tip vortices from aircraft has been a topic of considerable study over the past fifty years. A motivation for these investigations stems from their interaction with follower aircraft. The so-called wake–vortex hazard, in which an aircraft encounters the wake of a preceding aircraft, is a limiting factor for the capacity of airports around the world. Spalart (1998) provides an extensive review of airplane trailing vortices which details their persistence and evolution in the context of air travel. Further reviews by Crouch (2005) and Savas (2005) discuss efforts to control these trailing vortices, through passive and active means, in an attempt to accelerate their breakup or modify their strength.

Hummel (1983) has demonstrated positive consequences for the interaction of a trailing vortex with a wing, which can provide significant energy savings as a result of increased aerodynamic performance. Lissaman & Schollenberger (1970) shows this is attributed to a reduction in induced drag and an associated increase in the lift to drag ratio. The formation flight of aircraft and birds takes advantage of this concept. Apart from the enhancement in aerodynamic performance, it is known that vortices

† Email address for correspondence: gef213@lehigh.edu

impinging on a wing or blade can induce unsteady pressure fluctuations along their surfaces, resulting in unsteady loading and/or disruption of its flight path. Rockwell (1998) reviews the origins of loading on a body in relation to the physics of the vortex interaction. Further insight into recent advances in the area of vortex–wing interactions, with emphasis on the related flow physics, are provided by Garmann & Visbal (2014), Barnes, Visbal & Gordnier (2015) and Garmann & Visbal (2015) and their previous works cited therein.

For all of the foregoing applications, the structure of the vortex incident upon the downstream wing or aircraft will influence the nature of the interaction and thereby the unsteady and steady loading. In the following, we first address previous related investigations of the near-field evolution of a vortex from a wing subjected to controlled motion, then we investigate the basic physics of unstable and perturbed vortices.

Vortex structure from wing or control surface subjected to controlled motion. Several investigations have focused on the near-field evolution of a vortex from an oscillating, or perturbed wing or control surface. Ramaprian & Zheng (1998) examined the evolution of a perturbed trailing vortex from a pitching wing using three-component laser Doppler velocimetry to characterize the distributions of velocity, vorticity and circulation. Chang & Park (2000) employed triple-hot-film probe measurements to address the axial and azimuthal velocity profiles in the near field of a trailing vortex behind a pitching rectangular wing. Birch & Lee (2005) investigated the three-dimensional flow structure behind a pitching rectangular wing a using a triple-hot-wire probe over a range of perturbation frequencies. Experimental investigations conducted by Panagakos & Lee (2006) and Lee (2007) used triple-hot-wire probe measurements to determine the effectiveness of an oscillating trailing-edge tab, located on the trailing corner of the wing, to control the strength of a tip vortex from a pitching rectangular wing. Similarly, the experiments of Gerontakos & Lee (2006) employed an actuated trailing-edge flap, across the entire wingspan, on a pitching rectangular wing in order to alter the structure of the wing-tip vortex.

Most recently, Garmann & Visbal (2016*a*) and Garmann & Visbal (2016*b*) have investigated the effect of heaving wing oscillations on the development of a wing-tip vortex. Their studies employed high-fidelity computations to examine the evolution of a vortex from a wing undergoing a low amplitude, high frequency perturbation with emphasis on its three-dimensional generation along the rounded wing tip. Enhanced separation, in conjunction with stretching of the vortex along the wing tip, produces significant fluctuations of the vortex core structure which persist into the wake of the wing. Associated spiralling substructures were apparent around the periphery of the vortex throughout a portion of the heaving cycle. At sufficiently large streamwise distance downstream of the wing, the amplitude of the vortex trajectory increased substantially with streamwise distance and self-induced orbital motion of the vortex became apparent.

When relatively large amplitude heaving or pitching motions of a wing occur, in contrast to the small amplitude wing perturbations of interest herein, the development of the flow structure along the wing is expected to influence the evolution of the tip vortices in the near-wake region. Visbal (2011) employed high-fidelity numerical simulations to investigate the flow structure along a heaving flat plate. Spiralling undulations in the structure of the wing-tip vortices were observed along the wing and into the wake. The wing-tip vortices undergo breakdown and reformation over the course of the heaving cycle and are associated with the formation and transport

of an arch-like vortex along the plane of symmetry of the wing. Experimental investigations of the flow structure along plunging wings undergoing large amplitude or high frequency motion have been carried out by Yilmaz & Rockwell (2010), Cleaver *et al.* (2011) and Calderon *et al.* (2013). These considerations are beyond the scope of the present investigation, which focuses on a small amplitude, low frequency perturbation of the wing and the resultant trailing vortex.

The trailing vortex, from a wing subjected to controlled motion may undergo wandering. Garmann & Visbal (2014) employed high-fidelity computations to explore the wandering of a streamwise-oriented vortex in the presence of a rectangular wing located downstream. They found that, although the prescribed motion of the vortex was in the lateral direction, the vortex developed self-induced motion in the vertical direction as it approached the wing. Such wandering strongly influenced the detailed physics of the vortex–wing interaction and the associated loading of the wing.

Instabilities of a vortex. Theoretical investigations of this class of vortex flows provide a conceptual framework for interpretation of the present experiments. Leibowich & Stewartson (1983) addressed the stability of a Batchelor (1964) (columnar) vortex with respect to three-dimensional perturbations. Their theory employed asymptotic instability analysis that led to a stability criterion related to the swirl ratio q of the vortex, which relates the peak swirl (azimuthal) velocity and the defect of axial velocity. They showed that for small values of q, the vortex is unstable with respect to azimuthal wavenumbers. Specifically, the amplification of small wavelength perturbations is precluded when $q > \sqrt{2}$. The consequence is that, below this threshold value of q, severe destabilization can occur for each of the azimuthal modes. Viola, Arratia & Gallaire (2016) review the evolution of investigations since the landmark contribution of Leibowich & Stewartson (1983), including Eckhoff (1984), Mayer & Powell (1992) and Delbende, Chomaz & Huerre (1998). Viola *et al.* (2016) also summarize advances on the topics of viscous core modes and occurrence of absolute instabilities. Both of these topics lie outside the scope of the present investigation. It is important, however, to determine whether there is potential for occurrence of an absolute instability (AI) as opposed to a convective instability (CI). Olendraru & Sellier (2002) defines absolute–convective transition curves for a range of Reynolds number. Most relevant for the present investigation are the transition curves for values of Reynolds number based on the defect of axial velocity $Re_{\Delta u} = 100$ and 667. For the values of wake defect employed herein, these transition curves indicate that the vortex remains convectively unstable for all values of swirl ratio q.

Computations have revealed the consequences of harmonic forcing of azimuthal modes. For the case of a parallel swirling jet flow, Delbende & Rossi (2005) observed several effects, among them the occurrence of flow relaminarization during part of the oscillation cycle. Viola *et al.* (2016) employed direct numerical simulation (DNS), along with theoretically based approaches, to examine the effects of harmonic forcing of a globally stable, non-parallel Batchelor vortex for extreme cases of initially infinitesimal and finite amplitude levels of forcing. The forcing acted on all three velocity components. The azimuthal mode structure of the vortex was found to be a strong function of the forcing frequency and, furthermore, influenced by the amplitude of the forcing.

Unexplored issues. The preceding investigations have provided valuable insight into the flow structure along wings subjected to controlled motions and the development of a columnar vortex susceptible to the onset of instability and/or in response to applied perturbations. To date, quantitative experimental insight via global imaging

into the structure of a perturbed trailing vortex has received little attention. The focus of the present investigation is on the following unexplored aspects of the physics of a trailing vortex subjected to a periodic, small amplitude perturbation having a wavelength much larger than the characteristic radius of the vortex: (i) the potential for large amplitude undulations of transverse displacement and circulation of the trailing vortex relative to small amplitude perturbation of the wing; (ii) associated variations of patterns of axial vorticity and axial velocity deficit, as well as the phase shift between them, along the vortex; (iii) the interrelationship between the onset of patterns of pronounced azimuthal vorticity in relation to patterns of axial vorticity and axial velocity deficit; (iv) the link between the foregoing aspects and the time-dependent variation of swirl ratio along the vortex; and (v) interpretation of the vortex response in terms of concepts of stability theory, in particular the role of the theoretical threshold condition of Leibowich & Stewartson (1983) in predicting the occurrence of elevated levels of azimuthal vorticity and the degree of its persistence in downstream regions of the trailing vortex, in relation to streamwise variations of axial velocity deficit and swirl ratio. These concepts are addressed via volumetric and cross-sectional representations of the vortex structure acquired from stereo particle image velocimetry (SPIV).

2. Experimental system and techniques

Experiments were conducted in a large-scale, recirculating water channel at Lehigh University. The main test section of the facility is 508 mm in depth and 613 mm in width. A sequence of honeycomb meshes and screens are arranged upstream of the test section in order to attain a turbulence intensity of less than 0.3 per cent. The free stream velocity was maintained at $U_\infty = 160$ mm s^{-1} which yields a chord based Reynolds number $Re_C = U_\infty C/\nu = 16\,000$, where C is the chord of the wing and ν is the kinematic viscosity of water. The Reynolds number based on the scale of the vortex circulation is $Re_\Gamma = \Gamma/\nu = 2300$, where Γ is the circulation of the vortex.

Stereoscopic particle image velocimetry was employed to determine the flow structure of a vortex from a continuously heaving wing. Figure 1(*a*) depicts a schematic of the system. The blockage ratio of the wing with respect to the cross-sectional area of the channel, taking into account the maximum amplitude of excursion of the wing motion, is 0.01 or 1 %, which is well within the acceptable range for quality wind tunnel tests, as described by West & Apelt (1982). A laser sheet oriented in the spanwise direction, in conjunction with two charged coupled device (CCD) cameras, are used to capture the three-dimensional velocity field at successive cross-flow oriented planes. The cameras are arranged in an angular displacement configuration as shown in figure 1(*a*). This arrangement employs the Schiempflug condition which requires that the image plane, object plane and lens plane be coplanar as described by Prasad (2000). This ensures uniform focus across the image plane. Additionally, two prisms filled with distilled water are placed on the sides of the channel walls in order to mitigate the effects of refraction.

Figure 1(*b*) shows a schematic of the mechanism used to perturb the wing. It involves a computer-controlled motor that drives a scotch-yoke mechanism attached to the sting of the wing. The sting is located at the mid-span and mid-chord of the wing. It is fastened to a sliding bar that is coupled to a vertically oriented traverse. A connecting rod is used to fix the sliding bar to a wheel attached to the motor. The position of the wing is controlled through the feedback of an encoder attached to the motor.

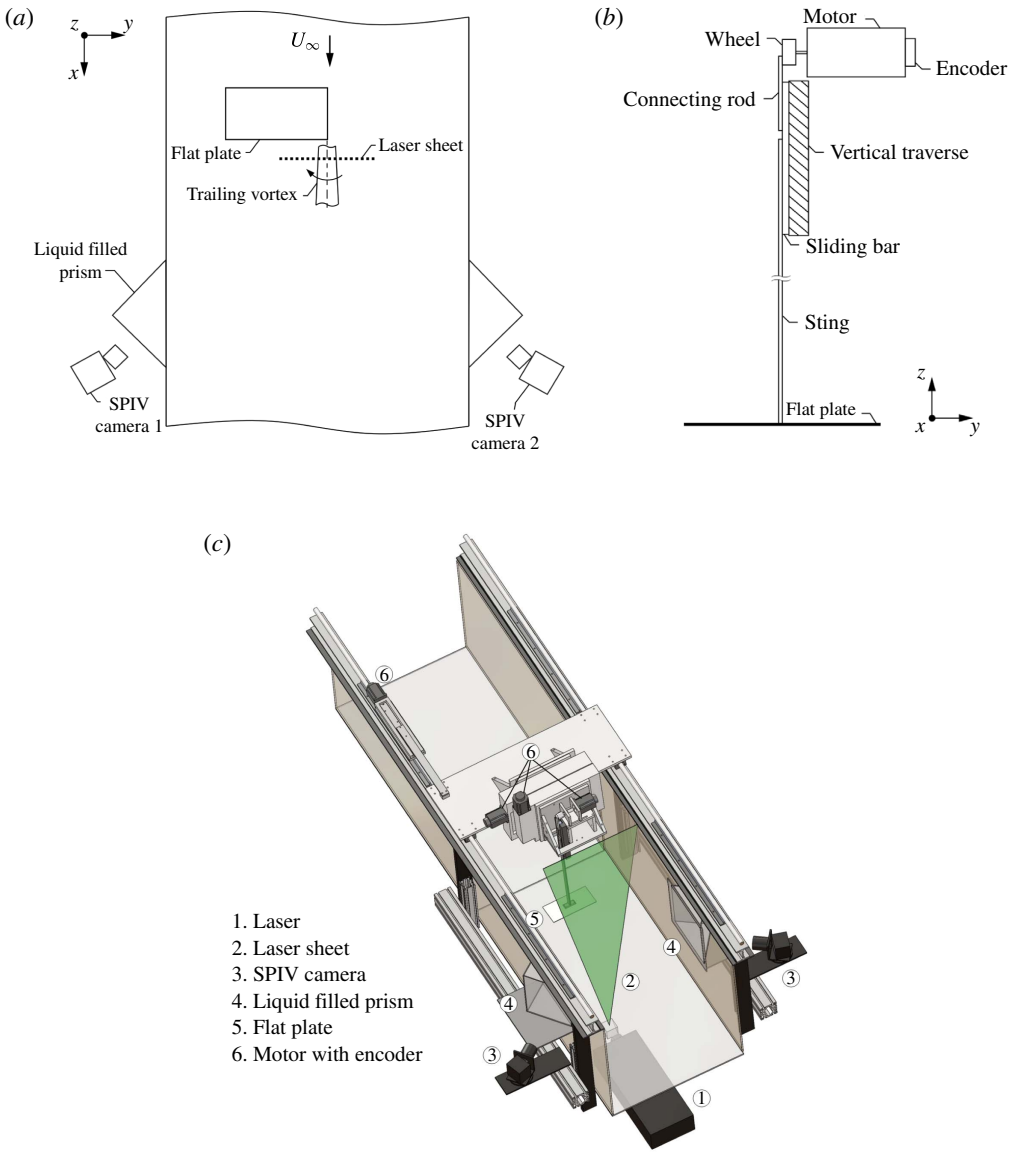

FIGURE 1. (Colour online) (*a*) Schematic of stereo particle image velocimetry system. (*b*) Schematic of wing oscillation mechanism (not to scale). (*c*) Model of test section and experimental system.

Figure 1(*c*) is a rendered model of the test section that includes the SPIV system, the wing perturbation mechanism and the wing positioning system. The laser head is positioned underneath the channel and the laser sheet is oriented in the spanwise direction. The wing positioning system consists of several motors with encoders that allow for precise positioning of the wing in all three directions, in addition to the controlled perturbation described previously. In order to capture images at successive planes in the streamwise direction, the motion control system is translated along a rail system which extends the length of the channel.

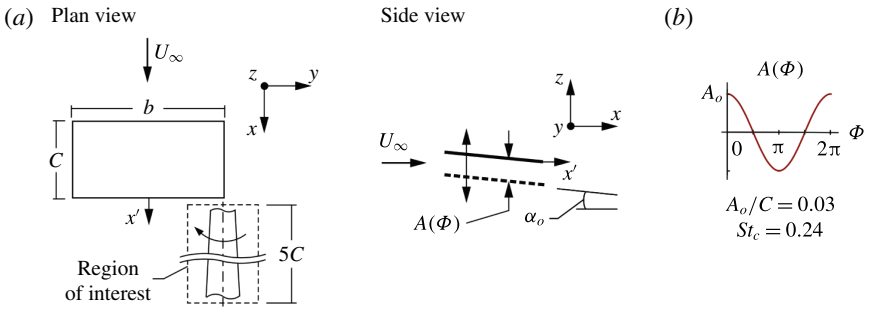

FIGURE 2. (Colour online) (*a*) Plan and side view schematics of wing. (*b*) Motion profile of wing.

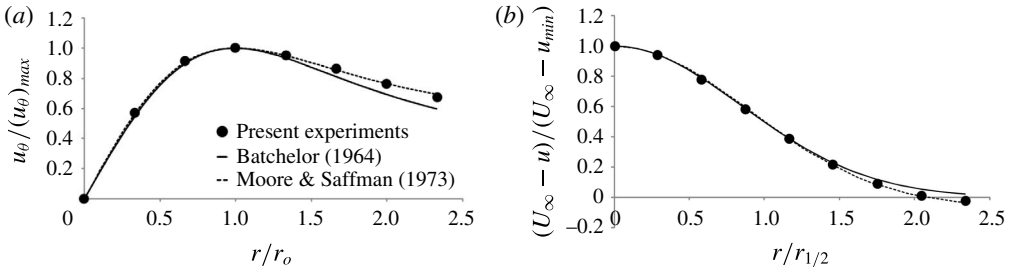

FIGURE 3. Comparison of normalized azimuthal velocity $u_\theta/(u_\theta)_{max}$ profiles as a function of vortex radius r_o (*a*) and normalized axial velocity deficit $(U_\infty - u)/(U_\infty - u_{min})$ as a function of the radial half-width of the vortex $r_{1/2}$ (*b*).

Plan and side view schematics of the experimental system can be seen in figure 2(*a*). The model of the wing is a rectangular flat plate of aspect ratio $AR = 2$, with a chord $C = 102$ mm and span $b = 203$ mm. The thickness of the wing $t = 1.6$ mm and the corner radius $r_c = 0.5$ mm. The wing is fixed at an angle of attack $\alpha_o = 6°$ and is subjected to continuous heaving motion in the vertical direction as indicated in the side view schematic. The region of interest extends 5 chords into the wake of the wing. Figure 2(*b*) depicts the sinusoidal displacement amplitude $A(\Phi)$ of the wing as a function of phase angle Φ. The oscillation cycle consists of the downstroke of the wing which occurs between $\Phi = 0$ to $\Phi = \pi$ and the upstroke between $\Phi = \pi$ to $\Phi = 2\pi$.

The non-dimensional Strouhal number of the continuous wing motion, indicated in figure 2(*b*), is $St_c = fC/U_\infty = 0.24$, or $St_A = fA_o/U_\infty = 0.007$, where f is the oscillation frequency of the wing and A_o is the amplitude of the wing motion. This corresponds to a wavelength $\lambda/C = U_\infty/fC = 4.2$ or $\lambda/d_o = 42$, where d_o is the diameter of the vortex. That is, the wavelength associated with the wing motion is nearly two orders of magnitude larger than the vortex diameter. The vortex diameter d_o is defined as twice the vortex radius r_o, where r_o is the circumferentially averaged radial location where the maximum value of swirl velocity $(u_\theta)_{max}$ occurs. The displacement amplitude of the wing motion $A_o/C = 0.03$ or $A_o/d_o = 0.3$ and the corresponding velocity amplitude is $w_o/U_\infty = 0.04$.

The structure of the vortex from the tip of the stationary wing is given in figure 3, which provides experimental distributions of azimuthal velocity u_θ and axial velocity

deficit $U_\infty - u$ in comparison with the theories of Batchelor (1964) and Moore & Saffman (1973). The axial component of velocity is normalized by the peak axial velocity deficit $U_\infty - u_{min}$ in the vortex core and the half-width $r_{1/2}$, that is, the radius at which the axial velocity deficit is half of its peak value. The azimuthal component of velocity is normalized by the peak value $(u_\theta)_{max}$ and r_o, that is, the circumferentially averaged radial location where $(u_\theta)_{max}$ occurs. The normalized distributions of axial and azimuthal velocity for the present vortex agree well with the theoretical distributions of Moore & Saffman (1973). The distributions of Batchelor (1964) show deviations from the data in the outer region of the vortex.

The water is seeded with 11 μm metallic coated hollow plastic spheres. The density of the particles employed is 1.9589 g cm^{-3}. A dual pulsed Nd:YAG laser system is employed to generate a laser sheet of 1.5 mm thickness which illuminates the particles. Each of the CCD cameras used to capture the particle images contains an array of 1600 pixels × 1192 pixels. Interrogation windows of 32 pixels × 32 pixels are used and contain 15–20 particle images. A 50 % overlap between camera frames is utilized and the particle images are processed using a frame-to-frame cross-correlation technique. The effective resolution of the SPIV system employed is 14.92 pixels mm^{-1}. Uncertainty analysis of the in-plane velocity measurements was performed using the procedure described in Adrian & Westerweel (2011). The calculations yielded an in-plane velocity random error $\sigma_{\Delta V}$ that is 2.1 % of the free stream velocity. Lawson & Wu (1997) provides a relationship between the in-plane and out-of-plane errors. This yielded an out-of-plane random velocity error $\sigma_{\Delta U}$ that is 2.5 % of the free stream velocity.

During experiments, the laser sheet was oriented in the cross-flow direction, as previously indicated. Images were acquired at evenly spaced intervals in the streamwise direction for a total of 20 planes. The dimensionless distance between planes in the streamwise direction was $x'/C = 0.25$. A phase-referencing technique was employed, which grouped together images taken at a given vertical position of the wing; this process provided phase-averaged images. Instantaneous vortex centres were made coincident before performing time-averaged and phase-averaged calculations. Each plane yielded 7424 vectors, for a total of 148 480 vectors for volumetric reconstruction.

Volumetric reconstruction of the planar velocity field was performed using in-house software which interpolated and smoothed data between planes. Iso-surfaces of axial vorticity were smoothed using a method employed by Kim & Gharib (2010). The smoothed vorticity was calculated by $\omega_{new} = (\omega_{old} + \omega_{4avg})/2$, where $4avg$ is the mean of the four neighbouring vorticity values. This process was done one time. In order to assess the uncertainty in the volumetric reconstruction process, the theoretical solution of the Batchelor vortex, where viscous decay was incorporated as a function of streamwise distance, was used to compute theoretical patterns of velocity and vorticity. Over the continuous domain of the Batchelor vortex, sectional cuts of the vortex were taken at the equivalent streamwise intervals employed in the acquisition of experimental data. Linear interpolation between these planes was then performed to reconstruct volumes of velocity and vorticity. The foregoing smoothing method was then applied over the domain for axial vorticity. Corresponding deviations from the complete theoretical solution were then computed for velocity and vorticity. This process resulted in a maximum error of 1.1 % from the theoretical solution along the vortex.

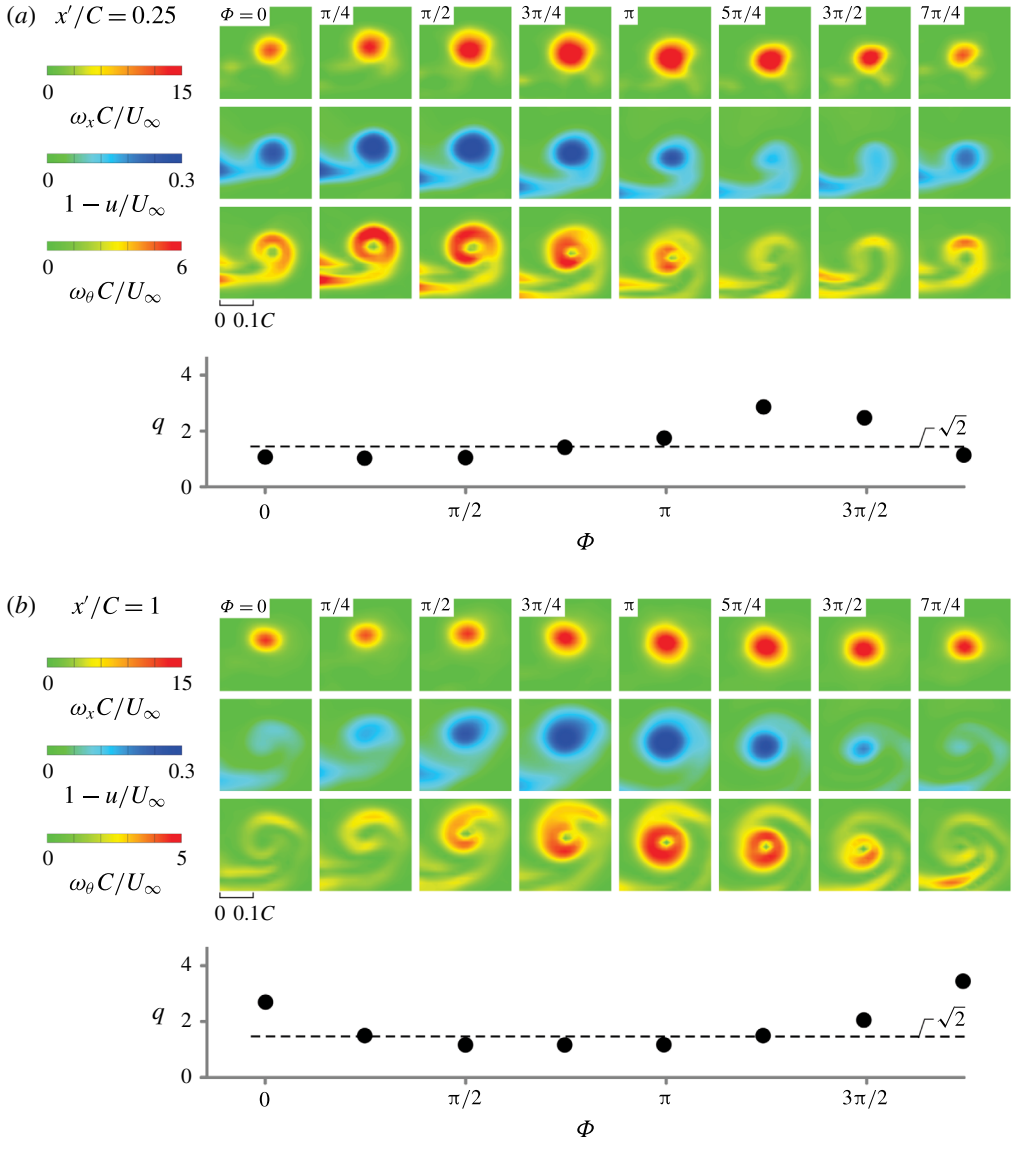

FIGURE 4. For caption see next page.

3. Unsteady vortex structure

3.1. *Sectional patterns of axial vorticity, axial velocity deficit and azimuthal vorticity*

Figure 4 shows cross-sectional patterns of normalized axial vorticity $\omega_x C/U_\infty$, axial velocity deficit $1 - u/U_\infty$ and azimuthal vorticity $\omega_\theta C/U_\infty$ as functions of phase angle Φ for streamwise distances (*a*) $x'/C = 0.25$, (*b*) $x'/C = 1$, (*c*) $x'/C = 3$ and (*d*) $x'/C = 5$. The cross-sectional patterns are oriented such that the streamwise direction is perpendicular to the page. Azimuthal vorticity is dominated by the in-plane derivatives of the velocity components; the contribution of out-of-plane components is negligible, as verified by detailed computations involving variable spacing between successive planes in the streamwise direction. The vertical position

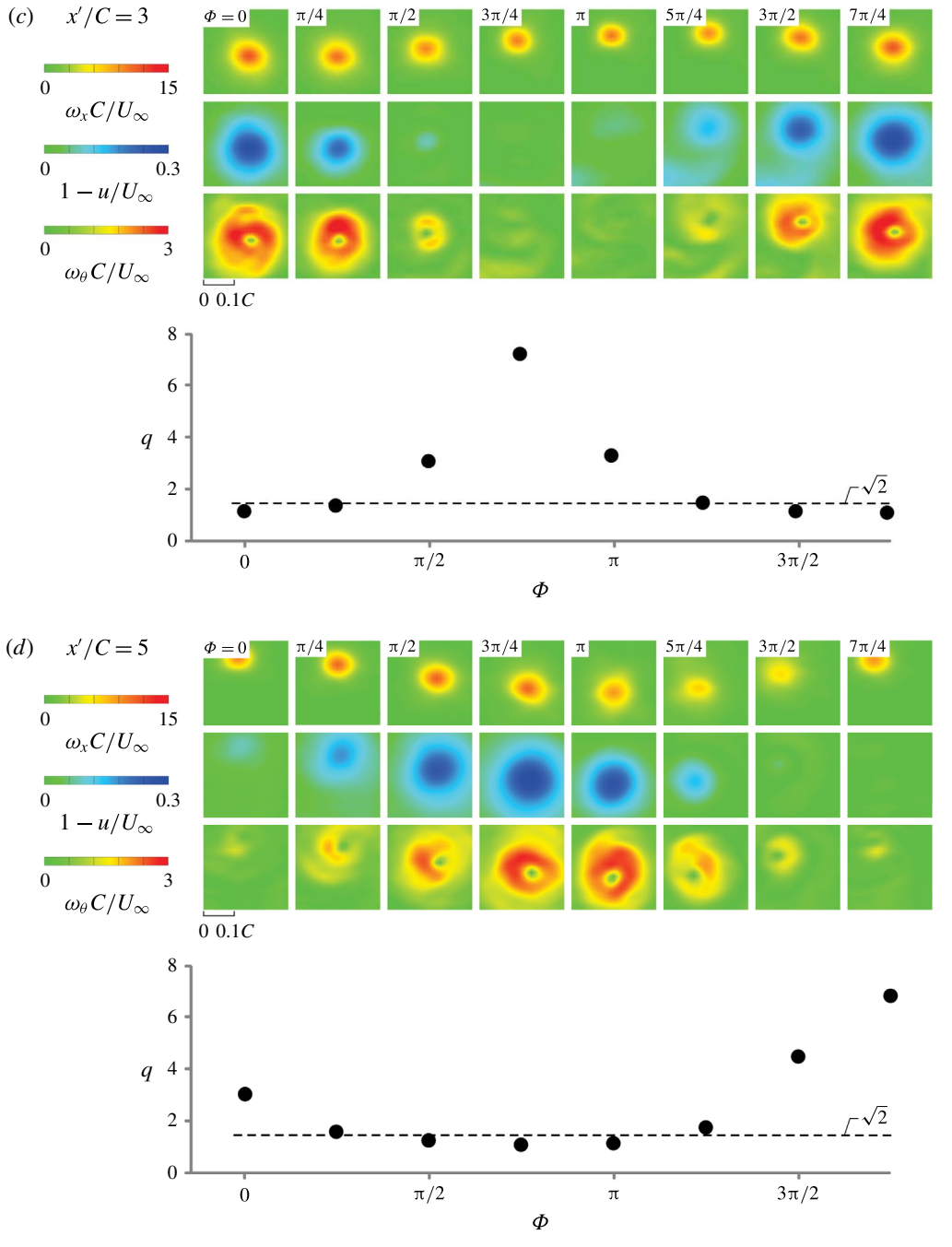

FIGURE 4 (cntd). (Colour online) Comparison of sectional cuts of axial vorticity $\omega_x C/U_\infty$, axial velocity deficit $1 - u/U_\infty$ and azimuthal vorticity $\omega_\theta C/U_\infty$ as functions of phase angle Φ for streamwise distances (*a*) $x'/C = 0.25$, (*b*) $x'/C = 1$, (*c*) $x'/C = 3$ and (*d*) $x'/C = 5$. A plot of the swirl ratio q as a function of Φ is also included.

of the wing defined in figure 2(*b*) is used as a phase reference in these images. The oscillation cycle consists of the downstroke of the wing which occurs between $\Phi = 0$ to $\Phi = \pi$ and the upstroke between $\Phi = \pi$ to $\Phi = 2\pi$.

All of the foregoing variations are a strong function of the swirl ratio q, which is plotted as a function of phase angle Φ at the bottom of figure 4. The stability properties of a vortex are dependent upon the swirl ratio q. As shown by Jacquin & Pantano (2002) it is defined as $q = \Gamma/2\pi r\Delta u = 1.567V_\theta/\Delta u$, where V_θ is the maximum azimuthal velocity and Δu is the peak axial velocity deficit within the vortex core. Leibowich & Stewartson (1983) determined the critical value of $q = \sqrt{2}$ for which excitation of azimuthal modes can occur. For larger values, when $q > \sqrt{2}$, rotation suppresses the perturbations and stabilizes the vortex, as indicated by Jacquin & Pantano (2002). As indicated by Viola *et al.* (2016), the entire range of azimuthal wavenumbers can be amplified when the condition $q < \sqrt{2}$ is attained, and the vortex becomes massively unstable. It is therefore anticipated that a substantial component of azimuthal vorticity may occur.

The images in figure 4(*a*), acquired at the location $x'/C = 0.25$, close to the trailing edge of the wing, indicate that the vertical displacement of the concentrations of axial vorticity, axial velocity deficit and azimuthal vorticity approximately follow the displacement of the wing, with a phase offset of $\pi/4$. That is, the displacement of the vortex centre position decreases from $\Phi = \pi/4$ to $\Phi = \pi$ and then increases from $\Phi = 5\pi/4$ back to $\Phi = 0$. At larger values of $x'/C = 1$, 3 and 5, the occurrence of maximum displacement shifts to larger values of $\Phi = \pi/2$, $5\pi/4$ and $7\pi/4$, respectively. This shift is associated with the convective speed of the induced disturbance along the axis of vortex which is of the order of the free stream velocity.

Furthermore, at $x'/C = 0.25$, the structure of the axial velocity deficit involves, for all values of phase angle, two regions: the core of trailing vortex, which has an approximately circular cross-section; and the wake of the wing associated with a nominally horizontal layer of velocity deficit. This combination results in distortion of the axial velocity deficit of the vortex, such that it is not completely circular. Additionally, it is evident that the increase and decrease of the strength of axial vorticity, axial velocity deficit and azimuthal vorticity are directly related to the position of the wing. During the downstroke, the magnitude and scale of the axial vorticity increase. However, during the upstroke, the converse occurs. This is also evident in the patterns of the axial velocity deficit and azimuthal vorticity. Significant levels of the magnitude and scale of the axial velocity deficit are present during the downstroke, yet decreased levels are apparent during the upstroke. While these features are approximately in phase, there is a discernible phase shift between occurrences of peak values of axial vorticity and axial velocity deficit, which will be further addressed in conjunction with figure 6.

The images at $x'/C = 0.25$ indicate that rings of azimuthal vorticity form around the centre of the vortex for phases $\Phi = 0$ to $\Phi = \pi$ in conjunction with enhanced levels of axial vorticity and axial velocity deficit. These developments occur below the critical value of swirl ratio $q = \sqrt{2}$. The temporal evolution, that is, the evolution with increasing phase Φ, of the azimuthal vorticity distribution is directly correlated to the magnitude and scale of the axial velocity deficit. A further observation is that at $\Phi = 0$, the concentration of azimuthal vorticity is not evenly distributed across the vortex. Enhanced azimuthal vorticity is evident along the top portion of the concentration indicated by darker levels of red. This region moves as an organized pattern around the vortex with increasing phase. When $\Phi = 3\pi/4$, the region of highest level azimuthal vorticity is located along the bottom portion of

the concentration. Subsequently, the level of azimuthal vorticity is attenuated during portions of the downstroke, from $\Phi = \pi$ to $3\pi/2$. However, at $\Phi = 7\pi/4$, when the value of swirl ratio falls below the critical value $q = \sqrt{2}$, re-formation of the region of peak azimuthal vorticity occurs along the top portion of the vortex. In essence, large magnitudes of the axial velocity deficit are associated with enhanced azimuthal vorticity, which evolve in an organized manner around the vortex. In fact, this observation holds for all streamwise distances x'/C as evident in subsequent image layouts.

At $x'/C = 1$, corresponding to the sets of images in figure 4(*b*), the structure and trajectory of the vortex, with respect to axial vorticity, are comparable to that at $x'/C = 0.25$. However, the nature of the axial velocity deficit has changed considerably. It is evident that its magnitude is not sufficiently large to be clearly detectable at all values of phase angle Φ, as is the case at $x'/C = 0.25$. That is, when $\Phi = 0$ and $\Phi = 7\pi/4$, the axial velocity deficit tends to zero. A pronounced axial velocity deficit is, however, present from $\Phi = \pi/4$ to $\Phi = 3\pi/2$. During these phases, the concentration of axial velocity deficit becomes detached from the wake of the wing and is elongated in the spanwise direction during the continuation of vortex roll up. Considering the entire oscillation cycle, it is evident that the phase shift between the magnitude and scale of the concentrations of axial vorticity and axial velocity deficit are approximately equivalent to that at $x'/C = 0.25$. In fact, this relationship also holds for larger values of $x'/C = 3$ and $x'/C = 5$, which are addressed in the following.

Moreover, the organized nature of the azimuthal vorticity patterns is also evident. When $\Phi = 0$, low-level azimuthal vorticity occurs along the top portion of the vortex. With increasing phase, it is evident that the region of peak azimuthal vorticity moves in a counter-clockwise orientation around the centre of the vortex. The significant changes of azimuthal vorticity are a consequence of the variation of swirl ratio. From $\Phi = 0$ to $\Phi = \pi/2$, the value of swirl ratio decreases below the critical value $q = \sqrt{2}$, and remains lower than $\sqrt{2}$ through $\Phi = \pi$. Correspondingly, the development of enhanced values of azimuthal vorticity is evident and the largest magnitude concentration occurs at $\Phi = \pi$. Conversely, from $\Phi = \pi$ to $\Phi = 7\pi/4$, the strength of azimuthal vorticity decreases as the swirl ratio value increases.

Common observations can be made for the images at $x'/C = 3$ and $x'/C = 5$, which are shown respectively in figure 4(*c*,*d*). It is apparent that the levels of axial vorticity within the vortex are attenuated relative to the levels at $x'/C = 0.25$ and $x'/C = 1$. Furthermore, the magnitude of the axial velocity defect is not discernible across a substantial share of the oscillation cycle. At values of Φ where the axial velocity deficit is evident, it has increased considerably in scale (spatial extent) and has become more circular in shape, relative to the patterns of velocity defect shown at $x'/C = 0.25$ and 1. Moreover, the scale of the azimuthal vorticity concentration has increased as well. It is again evident that the generation of enhanced azimuthal vorticity coincides with lower values of swirl ratio and the largest magnitude concentrations of azimuthal vorticity occur where the swirl ratio is below the critical value $q = \sqrt{2}$.

The trajectory of the vortex at larger values of $x'/C = 3$ and $x'/C = 5$ has distinct features, relative to its initial form at $x'/C = 0.25$ where it is solely in the vertical direction, as induced by the continuously heaving perturbation of the wing. At these larger values of x'/C, the amplitude of the vortex motion in the vertical direction increases with streamwise distance, but the vortex also develops motion in the spanwise direction. This is evident by comparing the position of the vortex centre at each phase angle. At $x'/C = 5$, from $\Phi = 0$ to $\Phi = 3\pi/4$, the vortex centre moves towards the right. However, from $\Phi = \pi$ to $\Phi = 7\pi/4$, the vortex centre moves in the

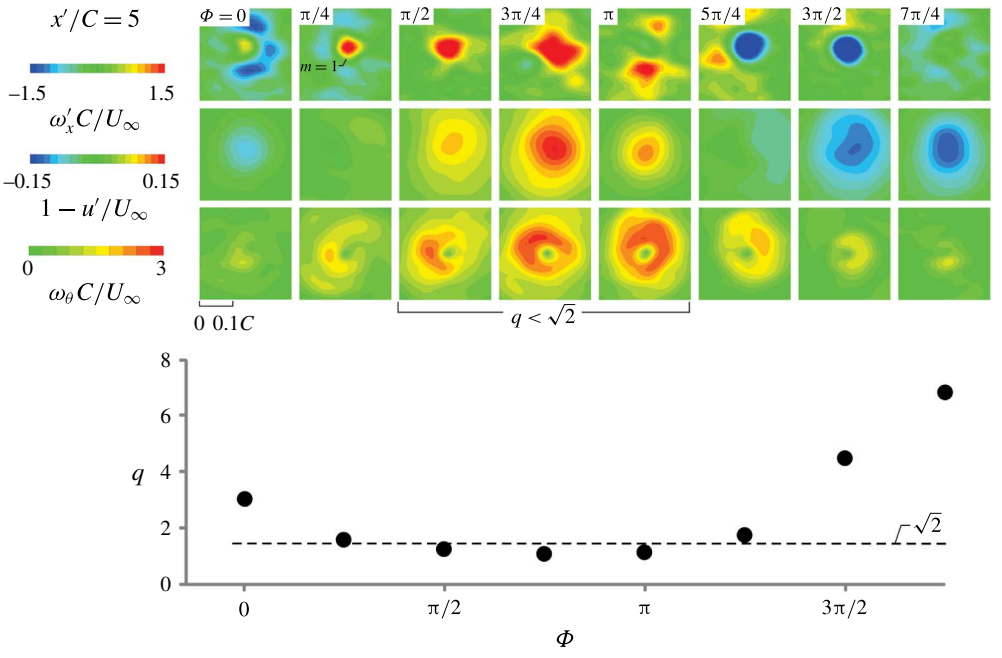

FIGURE 5. (Colour online) Sectional contours of axial vorticity fluctuations $\omega_x' C/U_\infty$, axial velocity deficit $1 - u'/U_\infty$ fluctuations and azimuthal vorticity $\omega_\theta C/U_\infty$ as functions of Φ at the streamwise distance $x'/C = 5$. A plot of the swirl ratio q as a function of Φ is also included.

opposite direction. In essence, the trajectory of the vortex transitions from a purely vertical motion to an orbital motion with increasing streamwise distance.

3.2. *Fluctuations of axial vorticity and axial velocity deficit*

Further insight into the undulation of the vortex and the generation of enhanced azimuthal vorticity $\omega_\theta C/U_\infty$ is shown in figure 5. It indicates the structure of instantaneous fluctuations of axial vorticity $\omega_x' C/U_\infty$ and axial velocity deficit $1 - u'/U_\infty$ from the time-averaged values as a function of phase angle Φ at the streamwise location $x'/C = 5$. These fluctuations are calculated respectively according to $\omega_x'(\Phi) = \omega_x(\Phi) - \overline{\omega_x}$ and $u'(\Phi) = u(\Phi) - \overline{u}$, where $\overline{\omega_x}$ and $\overline{u}$ are the time-averaged (mean) values. Prior to performing the foregoing calculations, the centres of the instantaneous and time-averaged vortex patterns were aligned such that they were coincident. The consequences of the variations of patterns of $\omega_x' C/U_\infty$ and $1 - u'/U_\infty$ on images of total azimuthal vorticity $\omega_\theta C/U_\infty$ are given in the third row of figure 5. All of the foregoing variations are a strong function of the swirl ratio q, which is plotted as a function of phase angle Φ at the bottom of figure 5.

In figure 5, an identifiable, small concentration of positive fluctuation of axial vorticity occurs at $\Phi = 0$. This dominant (red–yellow) structure, designated as $m = 1$ at $\Phi = \pi/4$, is amplified in both vorticity level and scale for successive values of phase angle $\Phi = \pi/4$, $\pi/2$ and $3\pi/4$, which indicates the winding of the vortex in the positive sense, that is, in the same direction as the concentration of total vorticity shown in figure 4(*d*). At these values of Φ, the magnitude of the swirl ratio is at or below the critical value of $q = \sqrt{2}$. This evolution of the instantaneous vorticity

fluctuation $\omega_x' C/U_\infty$ represents amplification of the $m = 1$ mode. The large-scale, positive (red–yellow) pattern of $\omega_x' C/U_\infty$ becomes distorted at $\Phi = 3\pi/4$, and at $\Phi = \pi$, it is severely disrupted, that is, partitioned into two (red–yellow) concentrations of vorticity fluctuations, with low-level vorticity fluctuations of opposite sign evident between them. The disruption of the coherent pattern of $\omega_x' C/U_\infty$ coincides with generation of enhanced azimuthal vorticity indicated in the third row of images. The amplification, distortion and eventual disruption of the $m = 1$ mode occurs when $q < \sqrt{2}$ in accord with the theoretical criterion of Leibovich & Stewartson (1983). At $\Phi = 3\pi/4$, the largest magnitude of the fluctuation of axial velocity deficit occurs. Remnants of the disrupted $m = 1$ mode are evident in the separated (red–yellow) clusters of $\omega_x' C/U_\infty$ at $\Phi = 5\pi/4$, but the major observation is that a negative (blue) circular concentration of $\omega_x' C/U_\infty$ abruptly occurs and this negative concentration of $\omega_x' C/U_\infty$ persists at $\Phi = 3\pi/2$; which occurs in conjunction with an increase of the swirl ratio. This negative concentration indicates winding of the vortex in the negative sense, that is, in the opposite direction of the concentration of total vorticity shown in figure 4(*d*). At $\Phi = 7\pi/4$, it has abruptly degenerated, leaving only a low-level, negative (blue) arc-like pattern of $\omega_x' C/U_\infty$ which persists until $\Phi = \pi/4$.

In summary, the foregoing observations are related to changes of the swirl ratio q depicted at the bottom of figure 5. From $\Phi = 0$ to $\Phi = 3\pi/4$, the value of q decreases and the scale of the (red) concentration of $\omega_x' C/U_\infty$ increases. When the swirl ratio reaches its minimum value, at $\Phi = 3\pi/4$, distortion of the coherent pattern of $\omega_x' C/U_\infty$ occurs and further disruption is evident at $\Phi = \pi$. At $\Phi = 5\pi/4$, the value of q has started to increase, and the abrupt onset of a concentrated (blue) core of $\omega_x' C/U_\infty$ is evident, as described in the foregoing. This concentrated core persists as the value of q continues to increase, then rapidly degenerates when a sufficiently large value of q is attained at $7\pi/4$. In essence, when the swirl ratio decreases with respect to Φ, rapid amplification of the vorticity fluctuations $\omega_x' C/U_\infty$ is evident. Disruption of the pattern occurs when the swirl ratio reaches the minimum value, corresponding to attainment of the maximum positive value of instantaneous velocity deficit $1 - u'/U_\infty$, and in association with large concentrations of azimuthal vorticity $\omega_\theta C/U_\infty$. Conversely, when the swirl ratio increases with respect to increase of Φ, patterns of vorticity fluctuations $\omega_x' C/U_\infty$ with a well-defined core occur, and eventually its rapid degeneration are evident at attainment of the maximum negative value of instantaneous velocity deficit $1 - u'/U_\infty$.

Conceptual insight into the patterns of $\omega_x' C/U_\infty$ over the range of phase angle Φ from 0 to π given in figure 5 is provided by Viola *et al.* (2016). They considered computations and theoretical interpretations of the nonlinear response of a non-parallel Batchelor vortex subjected to harmonic excitation in the form of streamwise perturbations of velocity for a range of amplitude and frequency, with the recognition that convective instability of the imposed perturbation can be amplified for a range of azimuthal wavenumbers when the swirl number is less than $q = 1.5$, thereby leading to massive destabilization. Computations showed that the most robust mode corresponded to $m = 1$ when the amplitude of excitation is 10 % of the free stream velocity. In the computations of Viola *et al.* (2016), the $m = 1$ mode takes the form of a dominant single concentration of vorticity having an axisymmetric (circular) shape, as a result of nonlinear distortion; it is similar to that shown in figure 5 and is prevalent at the dimensionless frequency of excitation $\omega_f = 0.5$. In the present experiments, the dimensionless frequency of excitation is $2\pi f r_o/\Delta u = 0.49$, and the amplitude is 15 % of the free stream velocity for the images of figure 5 where the $m = 1$ mode is dominant.

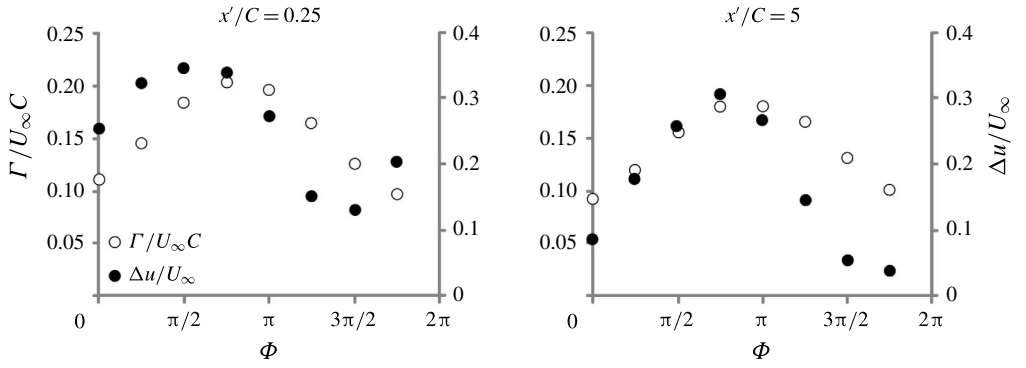

FIGURE 6. Comparison of plots of circulation $\Gamma/U_\infty C$ and peak axial velocity deficit $\Delta u/U_\infty$ at $x'/C = 0.25$ and $x'/C = 5$.

3.3. *Fluctuations of circulation and axial velocity deficit*

The foregoing variations of the vortex structure indicated in figure 4 are further characterized in figure 6, which shows plots of vortex circulation $\Gamma/U_\infty C$ and peak values of axial velocity deficit $\Delta u/U_\infty = 1 - u_{min}/U_\infty$ as functions of phase angle Φ for axial distances $x'/C = 0.25$ and $x'/C = 5$. Circulation is calculated by employing a contour integral of velocity over a rectangular boundary encompassing the vortex, such that all of its axial vorticity is contained within the boundary. Overall, it is evident that the circulation and axial velocity deficit of the vortex undergo substantial, time-dependent fluctuations, even though the controlled perturbation of the wing has a very small amplitude. These fluctuations, while not entirely sinusoidal, exhibit a phase relationship between their peak values that persists throughout the flow field. The peak amplitude of the axial velocity deficit leads the peak of circulation. This also holds for intermediate streamwise distances.

In figure 6, instantaneous deviations from time-averaged values of circulation $\overline{\Gamma}/U_\infty C$ and peak axial velocity deficit $\overline{\Delta u}/U_\infty$ were determined. At $x'/C = 0.25$, the peak deviation of circulation is $\Gamma'/\overline{\Gamma} = 43\,\%$ from the time-averaged circulation $\overline{\Gamma}/U_\infty C = 0.14$ of the perturbed vortex. The peak deviation of axial velocity deficit $\Delta u'/\overline{\Delta u}$ similarly fluctuates in magnitude by 47 % from the time-averaged value $\overline{\Delta u}/U_\infty = 0.25$. At $x'/C = 5$, the peak fluctuation of circulation $\Gamma'/\overline{\Gamma}$ deviates from the time-averaged value of $\overline{\Gamma}/U_\infty C = 0.13$ by 38 %. On the other hand, the peak deviation of axial velocity deficit $\Delta u'/\overline{\Delta u}$ is 106 % from the time-averaged value $\overline{\Delta u}/U_\infty = 0.15$. As previously indicated, the displacement amplitude A_o/C and velocity amplitude W_o/U_∞ of the wing are 0.03 and 0.04, respectively. Despite the relatively small perturbation amplitudes associated with the wing motion, the vortex undergoes larger fluctuations in circulation and axial velocity deficit by one to two orders of magnitude.

3.4. *Azimuthal vorticity on volume representations of axial vorticity and axial velocity deficit*

Figure 7 shows volumetric representations of the vortex constructed from sectional (planar) cuts of the three-dimensional velocity field. Surfaces of constant axial vorticity $\omega_x C/U_\infty$ and axial velocity deficit $1 - u/U_\infty$ are depicted for the indicated phase angles Φ. Along the volumes are cross-sectional cuts of azimuthal vorticity $\omega_\theta C/U_\infty$.

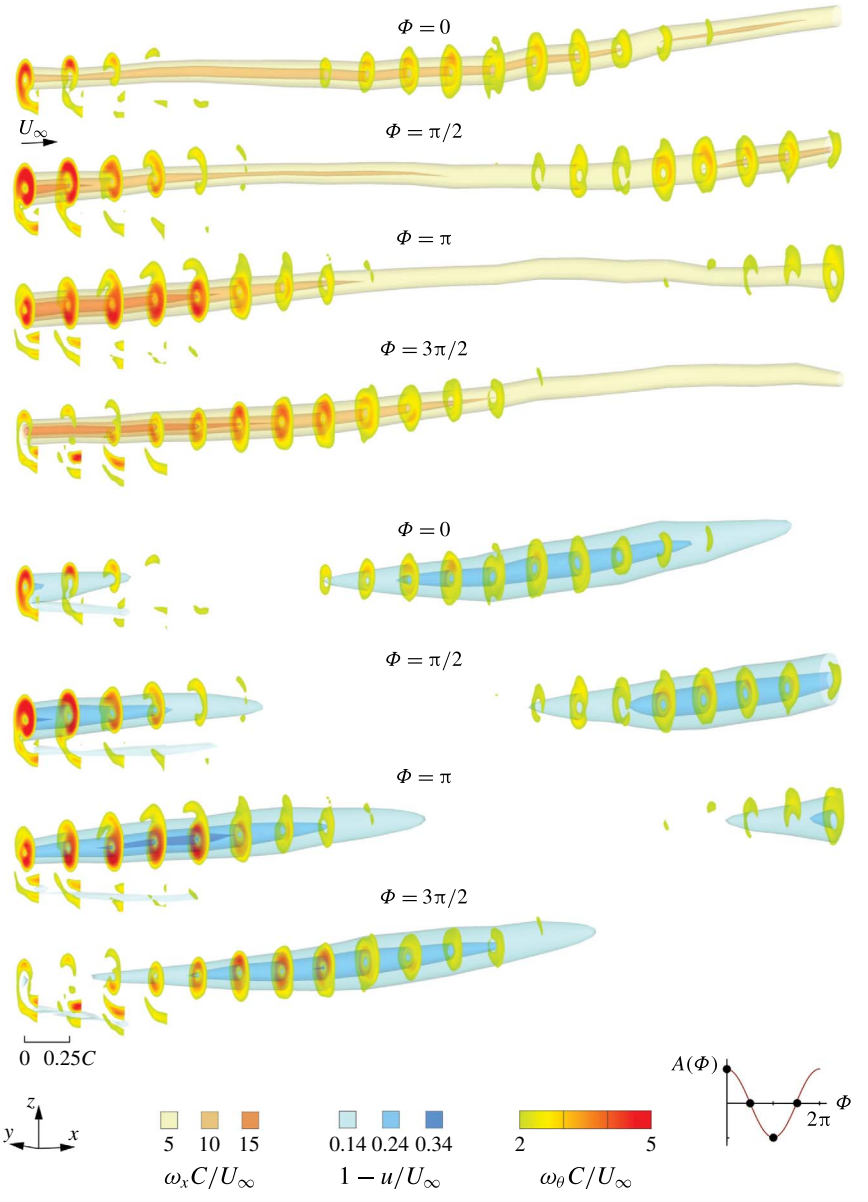

FIGURE 7. (Colour online) Comparison of iso-surfaces of axial vorticity $\omega_x C/U_\infty$ and axial velocity deficit $1 - u/U_\infty$ with sectional slices of azimuthal vorticity $\omega_\theta C/U_\infty$ as functions of phase angle Φ.

The images are oriented in a trimetric view and have been expanded in the vertical direction by a factor of 1.5 in order to resolve details. The field of view extends from $x'/C = 0.25$ to $x'/C = 5$. The small amplitude, long-wavelength perturbation of the wing has produced a vortex structure that consists of discrete regions of pronounced axial velocity deficit and azimuthal vorticity that travel through the vortex with a phase speed of the order of the free stream velocity.

Figure 7 also shows that large fluctuations of axial vorticity occur in the region immediately downstream of the trailing edge, which is consistent with the fluctuations indicated on the cross-sectional cuts of figure 4. In the volumetric representations of figure 7, fluctuations are represented by the change in colour of the vorticity levels, as well as their vertical and streamwise extent at successive values of phase angle Φ. During the downstroke of the wing, from $\Phi = 0$ to $\Phi = \pi$, large magnitude axial vorticity develops along the vortex centreline, but is attenuated at larger values of streamwise distance. As previously indicated in figure 4, the increase in magnitude of axial vorticity with phase angle approximately coincides with the generation of significant levels of axial velocity deficit along the centreline of the vortex in the region immediately downstream of the trailing edge. This process also induces significant levels of azimuthal vorticity about the periphery of the vortex. In the middle of the upstroke, at $\Phi = 3\pi/2$, remnants of the previously formed azimuthal vorticity persist in the region immediately downstream of the trailing edge while both the concentrations of azimuthal vorticity and the region of axial velocity deficit are attenuated as they convect downstream. This point is consistent with the sectional images of figure 4.

Furthermore, the concentrations of pronounced axial velocity deficit occupy distinct regions in space and propagate downstream through the centre of the vortex. As previously indicated in figure 6, fluctuations of circulation and axial velocity deficit in these regions can be one to two orders of magnitude larger than the imposed perturbation of the wing. It is important to note that the axial velocity deficit does not reach a magnitude corresponding to $\Delta u/U_\infty = 1 - u_{min}/U_\infty = 1$, i.e. there is no vortex breakdown. In effect, the wing perturbation produces, for a given phase angle, an internal structure of the vortex that consists of alternating regions of large axial velocity deficit and circulation, and regions of small to no axial velocity deficit and small circulation. The regions are accompanied by enhanced levels of azimuthal vorticity which form around the perimeter of the vortex.

3.5. *Occurrence of azimuthal vorticity on volume representations of axial velocity deficit: relation to swirl ratio*

The relationship between azimuthal vorticity $\omega_\theta C/U_\infty$, axial velocity deficit $1 - u/U_\infty$ and swirl ratio q is evident in figure 8, where the swirl ratio is plotted as a function of streamwise distance x'/C for selected values of Φ. A dashed black line is used to indicate the critical value $q = \sqrt{2}$. Superposed on these plots are iso-surfaces of axial velocity deficit with corresponding sectional cuts of azimuthal vorticity.

At each phase Φ, it is evident that in regions where $q < \sqrt{2}$, there are pronounced concentrations of axial velocity deficit and enhanced azimuthal vorticity. Moreover, the presence of azimuthal vorticity coincides with a decrease in swirl ratio, which is consistent with the cross-sectional patterns indicated in figure 4. As previously indicated, high-level azimuthal vorticity fluctuates in an organized manner about the centre of the vortex in these regions. When the swirl ratio of the vortex is larger than $\sqrt{2}$, no significant axial velocity deficit or azimuthal vorticity is present. Moreover, the value of swirl ratio can be as large as 14. In effect, this indicates that the axial velocity deficit along the vortex centreline can approach zero at certain phase angles, resulting in a locally stabilized region of the vortex, with no significant azimuthal vorticity. The combination of the foregoing observations indicates that the vortex structure is comprised of discrete regions of elevated values of azimuthal vorticity, circulation and axial velocity deficit, partitioned from regions in which

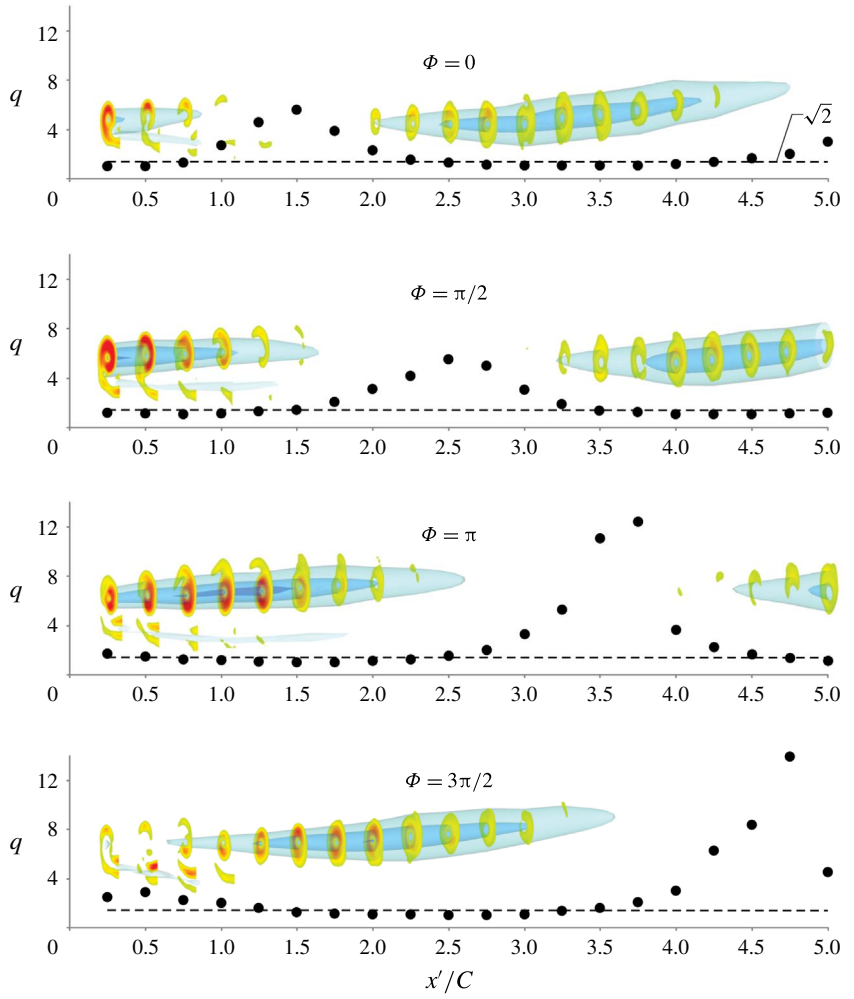

FIGURE 8. (Colour online) Plots of swirl ratio q as a function of streamwise distance x'/C with overlaying iso-surfaces of axial velocity deficit $1 - u/U_\infty$ and sectional cuts azimuthal vorticity $\omega_\theta C/U_\infty$ for selected phase angles Φ.

the foregoing features are not present. These regions containing elevated values of azimuthal vorticity, circulation and axial velocity deficit propagate downstream along the vortex.

4. Time-averaged vortex structure

4.1. *Sectional patterns of axial vorticity and axial velocity deficit*

Figure 9(*a*,*b*) shows selected cross-sectional patterns of normalized axial vorticity $\omega_x C/U_\infty$ and axial velocity deficit $1 - u/U_\infty$ for: (*a*) the unperturbed vortex (from a stationary wing) and (*b*) the time-averaged structure of the perturbed trailing vortex. It is evident that the imposed perturbation induces enhanced attenuation of the time-averaged vortex structure relative to the unperturbed vortex. At $x'/C = 1$, the patterns and levels of axial vorticity and axial velocity deficit for the unperturbed

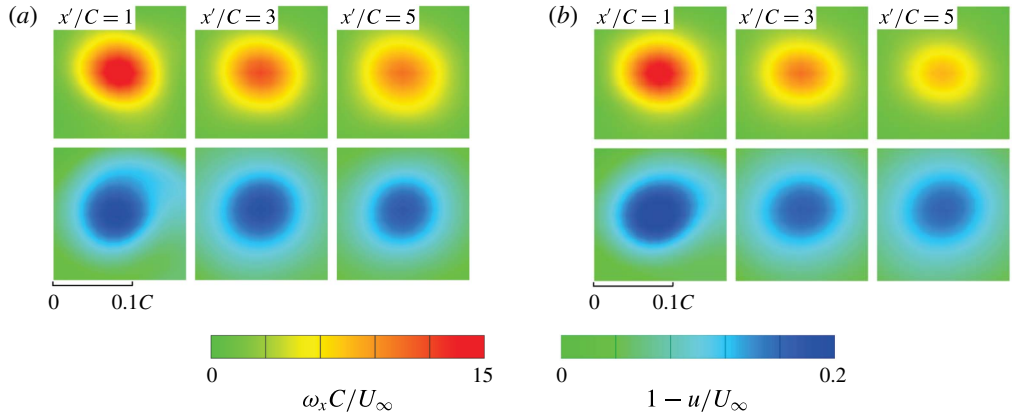

FIGURE 9. (Colour online) Comparison of sectional cuts of axial vorticity $\omega_x C/U_\infty$ and axial velocity deficit $1 - u/U_\infty$ as functions of streamwise distance x'/C for the (*a*) unperturbed and (*b*) perturbed vortex.

and perturbed vortices are very similar. However, it is apparent that the magnitudes of axial vorticity and axial velocity deficit attenuate more rapidly with streamwise distance for the case of the perturbed vortex.

4.2. *Volumetric representations of axial vorticity and axial velocity deficit*

The differences in flow structure between the unperturbed and perturbed vortices is further indicated in figure 10(*a*,*b*) which compares iso-surfaces of axial vorticity $\omega_x C/U_\infty$ and axial velocity deficit $1 - u/U_\infty$. It is evident that the larger values of axial vorticity attenuate more rapidly in the case of the perturbed vortex. However, in the region closest to the trailing edge, increased axial velocity deficit is evident in the perturbed vortex. Additionally, the maximum level of axial vorticity in the region immediately downstream of the trailing edge of the wing has decreased considerably for the perturbed vortex. Figure 10(*c*) shows plots of time-averaged, peak axial vorticity as a function of streamwise distance for the cases of the perturbed and unperturbed vortex. The difference in peak axial vorticity increases with streamwise distance. At $x'/C = 5$, the value of peak axial vorticity in the unperturbed vortex is 25 % greater than that of the perturbed vortex.

5. Conclusions

The structure of a trailing vortex from a wing undergoing very small amplitude, low frequency heaving motion is investigated using space–time images acquired via stereo particle image velocimetry. This perturbation, which has a long wavelength relative to the diameter of the vortex, leads to large undulations of axial velocity deficit $1 - u/U_\infty$ and circulation $\Gamma/U_\infty C$ along the vortex. Despite the small amplitude of the wing motion, instantaneous magnitudes of axial velocity deficit and circulation can reach values of the order of 50 % and 100 % greater than their respective time-averaged values.

At a given cross-section of the vortex, the magnitude of the time-dependent swirl ratio q undergoes large variations. As the minimum value of swirl ratio is approached, onset of pronounced azimuthal vorticity occurs and its pattern shows

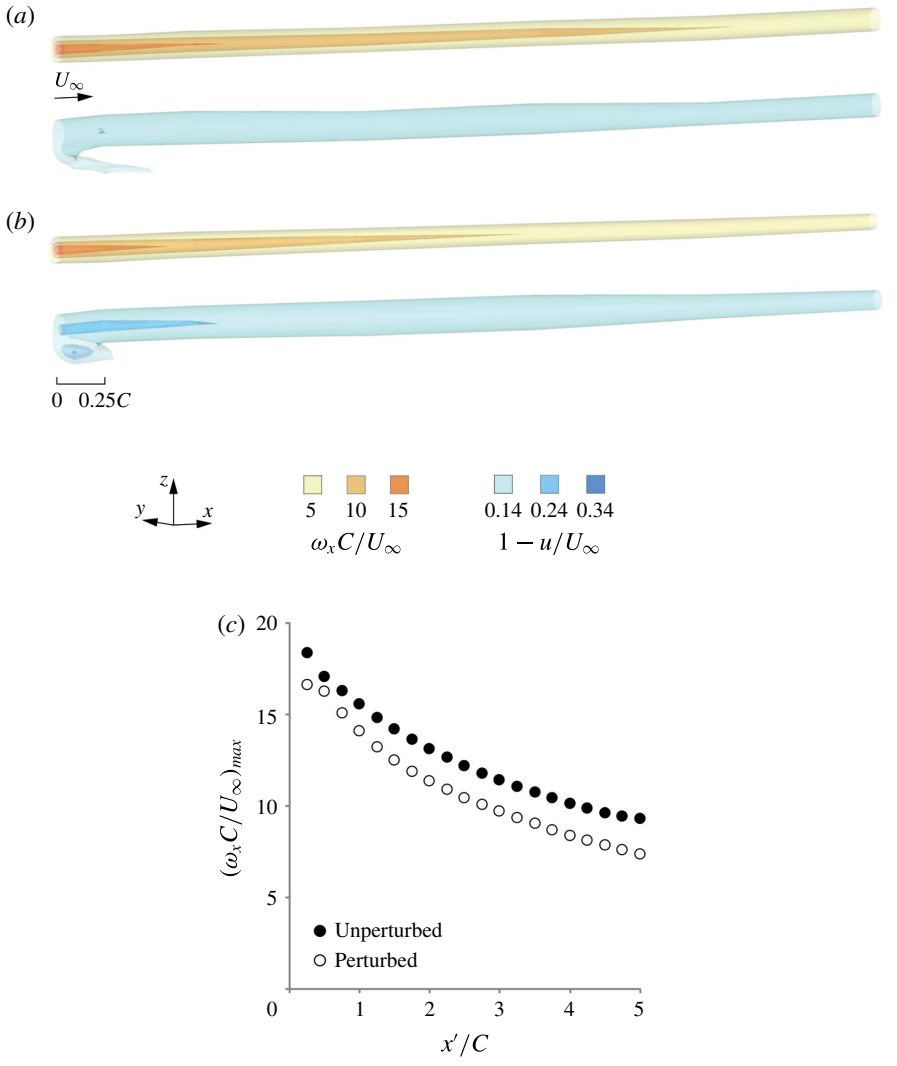

FIGURE 10. (Colour online) Iso-surfaces of axial vorticity $\omega_x C/U_\infty$ and axial velocity deficit $1-u/U_\infty$ for the (*a*) unperturbed and (*b*) perturbed vortex. (*c*) Plot of peak axial vorticity for the unperturbed and perturbed vortices.

the largest magnitude and scale when minimum swirl is attained. The onset of the pattern of azimuthal vorticity follows an orderly process of motion about the axis of the vortex until a ring-like structure occurs. Subsequently attenuation of the magnitude and scale of this pattern is evident. This process is closely correlated not only with the swirl ratio but also with the evolution of the pattern of axial velocity deficit; its largest magnitude and scale are in phase with the pattern of azimuthal velocity. This occurrence of elevated azimuthal vorticity is followed by regions of zero azimuthal vorticity that occur in conjunction with sufficiently large values of swirl ratio.

The foregoing characterizations at a given cross-section of the vortex have been confirmed by volumetric representations of the velocity defect and axial vorticity at selected instants (phase angles) of the wing perturbation; sectional patterns

of azimuthal vorticity are superposed on these volumetric representations. Spatial variations of these representations along the axis of the vortex emphasize the important consequence of streamwise variations of swirl ratio, in particular the largest magnitude and scale of the pattern of azimuthal vorticity occurs at the minimum value of swirl ratio.

The theoretical analysis of Leibowich & Stewartson (1983) establishes that when the swirl ratio $q = \sqrt{2}$, a range of azimuthal wavenumbers may be amplified, potentially leading to massive destabilization. This criterion for q provides a remarkably consistent threshold for onset of pronounced azimuthal vorticity, for temporal variation of q at a given cross-section of the vortex and spatial variation of q along the vortex at a given instant. When the minimum value of q is attained and has a value less than $\sqrt{2}$, the magnitude and scale of the pattern of azimuthal vorticity are maximized.

Consideration of the instantaneous fluctuations of axial velocity and velocity deficit indicate that the onset of maximum magnitude and scale of azimuthal vorticity corresponds to the onset of disorder of the instantaneous axial vorticity. Comparison of the present experiments in the region of decreasing swirl ratio with the computations and theoretical interpretations of Viola *et al.* (2016) show that the same form of the $m = 1$ mode occurs in their computations and the present experiments. In the region of increasing swirl ratio, the experimental pattern of instantaneous axial vorticity shows a highly concentrated and coherent core, corresponding to the restabilization, followed by eventual attenuation.

Acknowledgement

This investigation was supported by the AFOSR under grant FA9550-14-1-0166, monitored by Dr D. Smith.

REFERENCES

ADRIAN, R. J. & WESTERWEEL, J. 2011 *Particle Image Velocimetry*. Cambridge University Press.

BARNES, C. J., VISBAL, M. R. & GORDNIER, R. E. 2015 Analysis of streamwise-oriented vortex interactions for two wings in close proximity. *Phys. Fluids* **27**, 015103.

BATCHELOR, G. K. 1964 Axial flow in trailing line vortices. *J. Fluid Mech.* **20**, 645–658.

BIRCH, D. & LEE, T. 2005 Investigation of the near-field tip vortex behind an oscillating wing. *J. Fluid Mech.* **544**, 201–241.

CALDERON, D. E., WANG, Z., GURSUL, I. & VISBAL, M. R. 2013 Volumetric measurements and simulations of the vortex structures generated by low aspect ratio plunging wings. *Phys. Fluids.* **25**, 067102.

CHANG, J. W. & PARK, S. O. 2000 Measurement in the tip vortex roll-up region of an oscillating wing. *AIAA J.* **38**, 1092–1095.

CLEAVER, D. J., WANG, Z., GURSUL, I. & VISBAL, M. R. 2011 Lift enhancement by means of small-amplitude airfoil oscillations at low Reynolds numbers. *AIAA J.* **49**, 2018–2032.

CROUCH, J. D. 2005 Airplane trailing vortices and their control. *C. R. Phys.* **6**, 487–499.

DELBENDE, I., CHOMAZ, J. & HUERRE, P. 1998 Absolute/convective instabilities in the batchelor vortex: a numerical study of the linear impusle response. *J. Fluid Mech.* **355**, 229–254.

DELBENDE, I. & ROSSI, M. 2005 Nonlinear evolution of a swiriling jet instability. *Phys. Fluids.* **17**, 044103.

ECKHOFF, K. S. 1984 A note on the instability of columnar vortices. *J. Fluid Mech.* **145**, 417–421.

GARMANN, D. J. & VISBAL, M. R. 2014 Unsteady interactions of a wandering streamwise-oriented vortex with a wing. *AIAA Paper* 2014-2105.

GARMANN, D. J. & VISBAL, M. R. 2015 Interactions of a streamwise-oriented vortex with a finite wing. *J. Fluid Mech.* **767**, 782–810.

GARMANN, D. J. & VISBAL, M. R. 2016*a* Unsteady evolution of the tip vortex on a stationary and oscillating naca0012 wing. *AIAA Paper* 2016-0328.

GARMANN, D. J. & VISBAL, M. R. 2016*b* Further investigations of the tip vortex on an oscillating naca0012 wing. *AIAA Paper* 2016-4343.

GERONTAKOS, P. & LEE, T. 2006 Active trailing-edge flap control of oscillating-wing tip vortex. *AIAA J.* **44**, 2746–2754.

HUMMEL, D. 1983 Aerodynamic aspects of formation flight in birds. *J. Theor. Biol.* **104** (3), 321–347.

JACQUIN, L. & PANTANO, C. 2002 On the persistence of trailing vortices. *J. Fluid Mech.* **471**, 159–168.

KIM, D. & GHARIB, M. 2010 Experimental study of three-dimensional vortex structures in translating and rotating plates. *Exp. Fluids* **49**, 329–339.

LAWSON, N. J. & WU, J. 1997 Three-dimensional particle image velocimetry: error analysis of stereoscopic techniques. *Meas. Sci. Technol.* **8**, 897–900.

LEE, T. 2007 Effectiveness of dynamically deflected tab control of a tip vortex. *AIAA J.* **45**, 2994–3002.

LEIBOWICH, S. & STEWARTSON, K. 1983 A sufficient condition for the instability of columnar vortices. *J. Fluid Mech.* **126**, 335–356.

LISSAMAN, P. B. S. & SCHOLLENBERGER, C. A. 1970 Formation flight of birds. *Science* **168**, 1003–1005.

MAYER, E. W. & POWELL, K. G. 1992 Viscous and inviscid instabilities of a trailing vortex. *J. Fluid Mech.* **245**, 91–114.

MOORE, D. W. & SAFFMAN, P. G. 1973 Axial flow in laminar trailing vortices. *Proc. R. Soc. Lond.* A **333**, 491–508.

OLENDRARU, C. & SELLIER, A. 2002 Viscous effects in the absolute-convective instability of the batchelor vortex. *J. Fluid Mech.* **459**, 371–396.

PANAGAKOS, A. & LEE, T. 2006 Tip vortex control via an active trailing-edge tab. *J. Aircraft* **43**, 1152–1158.

PRASAD, A. K. 2000 Stereoscopic particle image velocimetry. *Exp. Fluids* **29**, 103–116.

RAMAPRIAN, B. R. & ZHENG, Y. 1998 Near field of the tip vortex behind an oscillating rectangular wing. *AIAA J.* **36**, 1263–1269.

ROCKWELL, D. 1998 Vortex-body interactions. *Annu. Rev. Fluid Mech.* **30**, 199–229.

SAVAS, O. 2005 Experimental investigations on wake vortices and their alleviation. *C. R. Phys.* **6**, 415–429.

SPALART, P. R. 1998 Airplane trailing vortices. *Annu. Rev. Fluid Mech.* **30**, 107–138.

VIOLA, F., ARRATIA, C. & GALLAIRE, F. 2016 Mode selection in trailing vortices: harmonic response of the non-parallel batchelor vortex. *J. Fluid Mech.* **790**, 523–552.

VISBAL, M. R. 2011 Three-dimensional flow structure on a heaving low-aspect-ratio wing. *AIAA Paper* 2011-219.

WEST, G. S. & APELT, C. J. 1982 The effects of tunnel blockage and aspect ratio on the mean flow past a circular cylinder with Reynolds numbers between 10^4 and 10^5. *J. Fluid Mech.* **114**, 361–377.

YILMAZ, T. O. & ROCKWELL, D. O. 2010 Three-dimensional flow structure on a maneuvering wing. *Exp. Fluids* **48**, 539–544.